

Gallium-Based Thin Films for Wearable Human Motion Sensors

Laurent Dejace, Nathan Laubeuf, Ivan Furfaro, and Stéphanie P. Lacour*

Wearable electronic circuits based on the films of gallium and its alloys offer promising implementations in health monitoring and gaming sensing applications. However, the complex rheology of liquid metals makes it challenging to manufacture thin gallium-based devices with reliable, reproducible, and stable properties over time. Herein, the surface coating and topography of silicone substrates are engineered to enable precisely defined, micrometer-thick liquid metal patterns over large ($>10\text{ cm}^2$) surface areas, and high design versatility. Control over the film microstructure meets manufacturing conditions that enable gallium films with a precise, repeatable, and durable electromechanical performance. The robustness and applicability of this technology in a virtual-reality scenario is demonstrated by implementing thin, soft, and stretchable gallium-based sensors to accurately monitor human hand kinematics.

Skin-mounted, wearable devices capable of monitoring the motion of the body are highly desirable for applications such as wellness, rehabilitation, and gaming.^[1,2] One of the key challenges in wearable technology is the ability to combine the desired device functionality with a satisfactory degree of integration with the body.^[3] To this end, soft and deformable electronic circuits leverage diverse technological combinations of materials, processing techniques, and integration strategies, with the goal of achieving mechanical compliance matching the complex deformation modes of the body. Recently, gallium-based liquid metals have emerged as candidate materials that combine high stretchability with low gauge factor and high electrical conductivity.^[4] Once embedded in silicone rubber, the liquid metal structures form highly deformable interconnects,^[5] antennas,^[6] and sensors.^[7] Additionally, gallium-based liquid metals


exhibit low toxicity^[8] and vapor pressure^[9] and therefore offer high handling safety, a property particularly suited for applications in contact with the body.

To deploy such technology^[10–20] outside of the laboratory environment, manufacturing and performance need to be precisely controlled, reliable, and repeatable over fabrication cycles and use. The high surface tension of gallium prevents the formation of homogeneous films on silicone carriers^[21] and hinders the control of the electrical properties at rest and under mechanical deformation. When exposed to oxidative environments, gallium immediately forms a solid $\approx 3\text{ nm}$ -thin oxide skin. This property has been leveraged to counterbalance surface tension and stabi-

lize the material, enabling the formation of metastable shapes.^[22] On the other hand, the amphoteric oxide skin hinders further processing as it can be removed only by reaction with acid or alkaline solutions,^[23] requiring the development of special patterning techniques adapted to the complex rheology of gallium.^[24] Processing solutions reported in the literature require either pressurizing the liquid metal and rupturing the oxide skin to enable shaping before the oxide skin regrowth,^[18,25–30] or removing the oxide skin in a reducing environment and allowing wetting of the liquid metal on a galliophilic pattern.^[31,32] Although promising, both approaches trade-off the patterning resolution with the ability to process large areas, leaving the capability of manufacturing complex gallium thin film patterns that can be employed for soft and stretchable circuits an unmet need.

In this context, a wafer-scale manufacturing technique enabling large-area gallium-based films to be patterned on silicone substrate with a fine control over the film microstructure and electromechanical performance is introduced. By engineering the topography and surface coating of the silicone polydimethylsiloxane (PDMS), thin and uniform liquid metal films are patterned by thermal evaporation and form stretchable electrical conductors (Figure 1a). Specifically, a textured PDMS substrate featuring a hexagonal lattice of round pillars with a sixfold axis rotational symmetry ($1.5\text{ }\mu\text{m}$ tall) is patterned by soft lithography and used as the base for the sputter deposition of a 40 nm gold film (Figure S1, Supporting Information). This serves as a wetting seed layer for the subsequent thermal evaporation of a gallium thin film ($m_{\text{Ga}} = 0.9\text{ mg cm}^{-2}$) in a vacuum chamber. Upon nucleation on the seed layer, gallium alloys with gold to form a thin, solid intermetallic phase (AuGa_2),^[33] then fills completely the inter-pillar volume as liquid phase (Figure 1b). At the end of the thermal evaporation process, the chamber is

L. Dejace, N. Laubeuf, I. Furfaro, Prof. S. P. Lacour
Bertarelli Foundation Chair in Neuroprosthetic Technology
Laboratory for Soft Bioelectronic Interfaces
Institute of Microengineering
Institute of Bioengineering
Centre for Neuroprosthetics
École Polytechnique Fédérale de Lausanne (EPFL)
Geneva 1202, Switzerland
E-mail: stephanie.lacour@epfl.ch

 The ORCID identification number(s) for the author(s) of this article can be found under <https://doi.org/10.1002/aisy.201900079>.

© 2019 The Authors. Published by WILEY-VCH Verlag GmbH & Co. KGaA, Weinheim. This is an open access article under the terms of the Creative Commons Attribution License, which permits use, distribution and reproduction in any medium, provided the original work is properly cited.

DOI: 10.1002/aisy.201900079

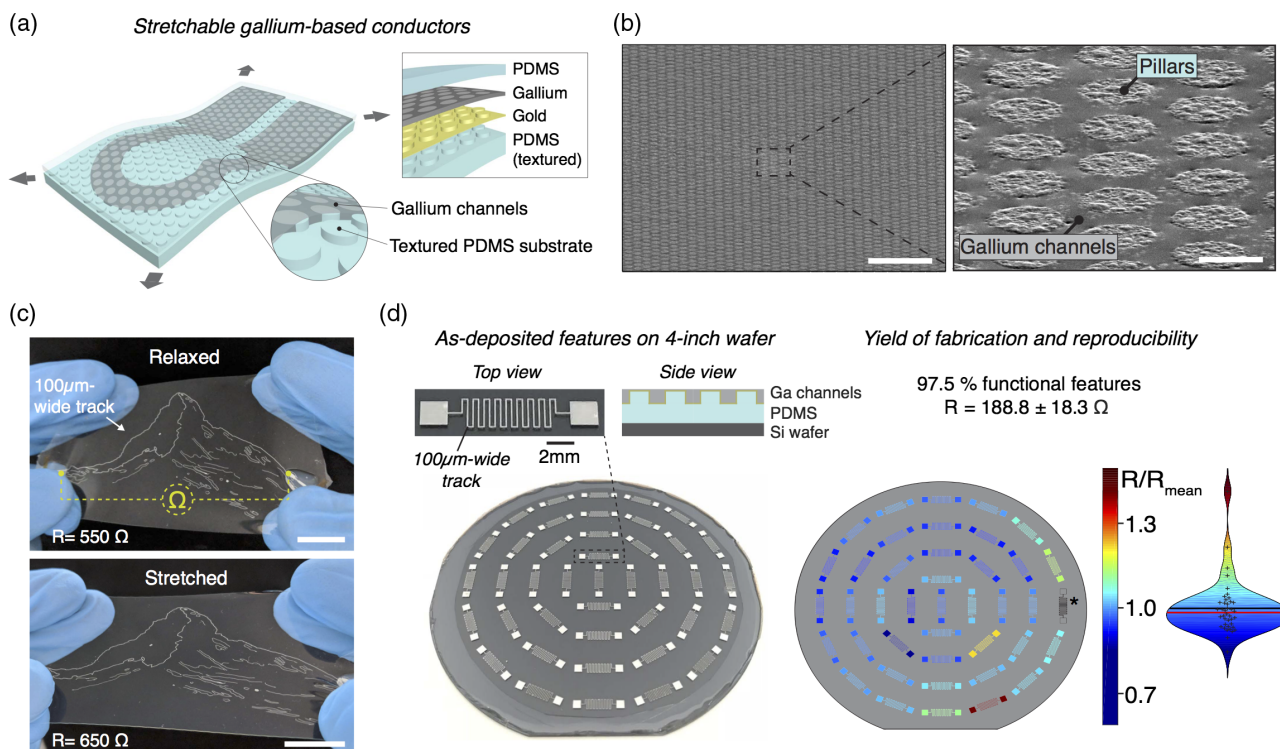


Figure 1. Stretchable gallium-based conductors. a) 3D scheme of a gallium-based electrical conductor embedded in PDMS. Inset–Exploded view of the layer stack: a textured PDMS substrate ($\approx 60\ \mu\text{m}$) coated with a 40 nm-thick sputtered gold film is used as the base for the thermal evaporation of a 1.5 μm -thick gallium metallization, further encapsulated with a solid PDMS layer ($\approx 60\ \mu\text{m}$). b) SEM images of liquid gallium channels confined in a hexagonal array of 1.5 μm -thick PDMS pillars. Scale bars: 50 μm (left), 5 μm (right). c) Photograph of a “Mount Matterhorn” pattern prepared with 100 μm -wide gallium tracks lithographically patterned on textured PDMS; the 7 cm-long track maintained stable electrical conduction when relaxed (top) and stretched (bottom) at $\approx 30\%$ strain. Scale bar: 1 cm. d) Photograph (left) of a 4-in. wafer onto which 100 μm -wide serpentine-shaped gallium features were patterned by photolithography. Schematic mapping (right) of the electrical resistance of each as-deposited feature, highlighting the resulting narrow distribution and high fabrication yield. *denotes the only defective pattern ($n = 41$).

vented to ambient pressure, such that the oxygen from the atmosphere promotes the formation of the oxide skin stabilizing the gallium morphology. A final PDMS encapsulation is bonded on the stack to further stabilize the system. The compatibility of this process with standard microfabrication techniques, such as photolithography, allows for precise patterning of the gold seed layer, which in turn enables complex gallium track geometries at the wafer-scale (Figure 1c and Figure S2, Supporting Information). This technique enables the fabrication of soft and stretchable conductive structures of any arbitrary design, with a minimum feature size of 10 μm defined by the smallest inter-pillar distance (Figure S3, Supporting Information), and a processing area limited by the wafer size (diameter = 10 cm). These structures offer mechanical robustness and remain electrically functional when reversibly deformed to large strains up to 50%. The high reproducibility of the gallium patterning process across the wafer was quantified by measuring the electrical resistance of serpentine structures patterned over a 4'' silicon wafer with 100 μm electrical line width (Figure 1d). The results show a narrow resistance distribution with a small wafer-scale non-uniformity ($R = 188.8 \pm 18.3\ \Omega$, $n = 41$) and a high fabrication yield of 97.5%.

The reliability and repeatability of the gallium thin film manufacturing process are optimized in view of their

implementation in wearable prototypes. To obtain uniform and completely filled PDMS microstructures with well-controlled electromechanical properties, we investigated the wetting dynamics of the liquid metal on various flat and textured, gold-coated PDMS substrates, by testing various geometrical parameters and process conditions. As observed in previous studies, thermal evaporation of gallium on the flat substrates leads to large and inhomogeneous liquid bulges (Figure 2a and Figure S4, Supporting Information),^[33] whereas deposition of gallium on textured substrates satisfying specific geometrical conditions leads to uniform and smooth films (Figure S5, Supporting Information).^[34,35] In agreement with the previous observations, wetting on the textured substrates occurred when

$$\tan(\theta) < h/L \quad (1)$$

where θ represents the contact angle of gallium droplets on flat, gold-coated PDMS ($\theta = 23^\circ$), h denotes the pillar height, and L the channel width (Figure S6, Supporting Information). Precise tuning of the channel width L allowed for the substrate lattice to be entirely filled with gallium, so as to obtain a smooth and homogeneous microstructure.

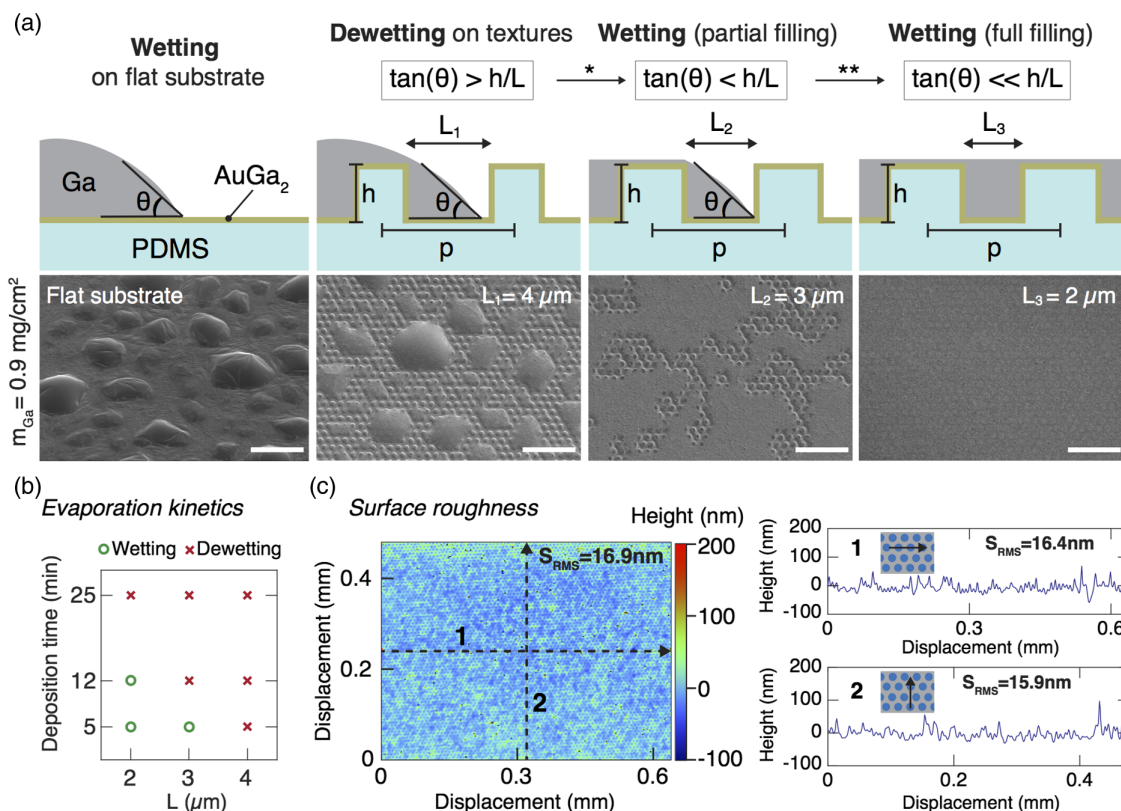


Figure 2. Substrate engineering for optimal gallium wetting. a) Cross-sectional scheme (top) and top-view SEM scans (bottom) of gallium evaporated on flat or textured, Au pre-coated PDMS substrates (deposition time: 5 min). On flat PDMS substrates, gallium alloys with the Au seed layer form a solid inter-metallic phase AuGa_2 and liquid gallium bulges with a contact angle $\theta = 23^\circ$. On textured substrates, patterned with a hexagonal lattice of round PDMS pillars (height $h = 1.5 \mu\text{m}$, pitch $p = 8 \mu\text{m}$), the dewetting to wetting transition (*) of gallium is defined geometrically by the channel width L . For $\tan \theta > h/L$, gallium bulges form on the top of the structure. For $\tan \theta < h/L$, gallium fills the texture up to their top. Eventually decreasing the channel width ($L = 2 \mu\text{m}$) enables to fill the textures entirely (**). Scale bars: $50 \mu\text{m}$. b) Kinetic optimization of the wetting regime depending on the evaporation time and the channel width L . c) Optical profilometry image (left) of gallium wetting a textured PDMS substrate ($L = 2 \mu\text{m}$ depicted in (a)) and height profiles (right) along the horizontal (1) and vertical (2) directions.

The effect of thermal evaporation kinetics on the wetting regime of gallium on the textured substrates (Figure 2b and Figure S7, Supporting Information) was also investigated. At high deposition rates (i.e., short evaporation time, $t = 5 \text{ min}$), wetting occurred consistently with Equation (1). However, a different behavior was observed for decreased deposition rates, as gallium dewetting from all the structures occurred when the evaporation time was increased to 25 min. This suggests that lower deposition rates alter the film growth mode by leaving more time for the nucleation and growth of isolated gallium droplets.^[36] In addition, the droplets may also shadow the empty surrounding regions as the substrate rotates in the evaporation chamber. For a pillar structure with $L = 2 \mu\text{m}$, the profile and surface roughness of the thin film were assessed next by optical profilometry (Figure 2c). The liquid metal films on textured substrates are smooth and well confined between the substrate pillars, and display a low surface roughness of 16.9 nm (root mean square [RMS]). The gallium films are therefore smooth and uniform, thereby less likely to suffer from microstructural evolution and changes in performance over time due to reactive wetting of the liquid metal (Figure S4, Supporting Information).^[37]

The electromechanical properties of the optimized gallium thin films ($L = 2 \mu\text{m}$) were then assessed to evaluate their potential implementation as soft sensors. At rest, the films display precise, narrow ($R = 0.43 \pm 0.02 \Omega \text{ sq}^{-1}$, $w = 300 \mu\text{m}$, $l = 15 \text{ mm}$, $n = 6$), and stable electrical resistance distributions over time ($t = 0, 3, 7, 14 \text{ days}$) (Figure 3a). The gallium films are confined in the textures thus no significant change in electrical resistance is observed after encapsulation with a PDMS layer (Figure S8, Supporting Information). The behavior under the deformation of non-encapsulated textured substrates was monitored during uniaxial mechanical stretching to 50% at different time intervals after manufacturing ($t = 0, 3, 7, 14 \text{ days}$) (Figure 3b and Figure S9, Supporting Information). The results suggest that the films maintain reproducible electromechanical properties over time, which is a highly desirable feature for device use after an idle shelf period. The gallium thin films exhibit reversible deformation, high linearity, low hysteresis, and unchanged baseline electrical resistance (Figure 3b). These characteristics confirm the benefits of confining gallium films in textures instead of depositing them on flat substrates (Figure S9 and S10, Supporting Information). The gallium thin films remain electrically functional when

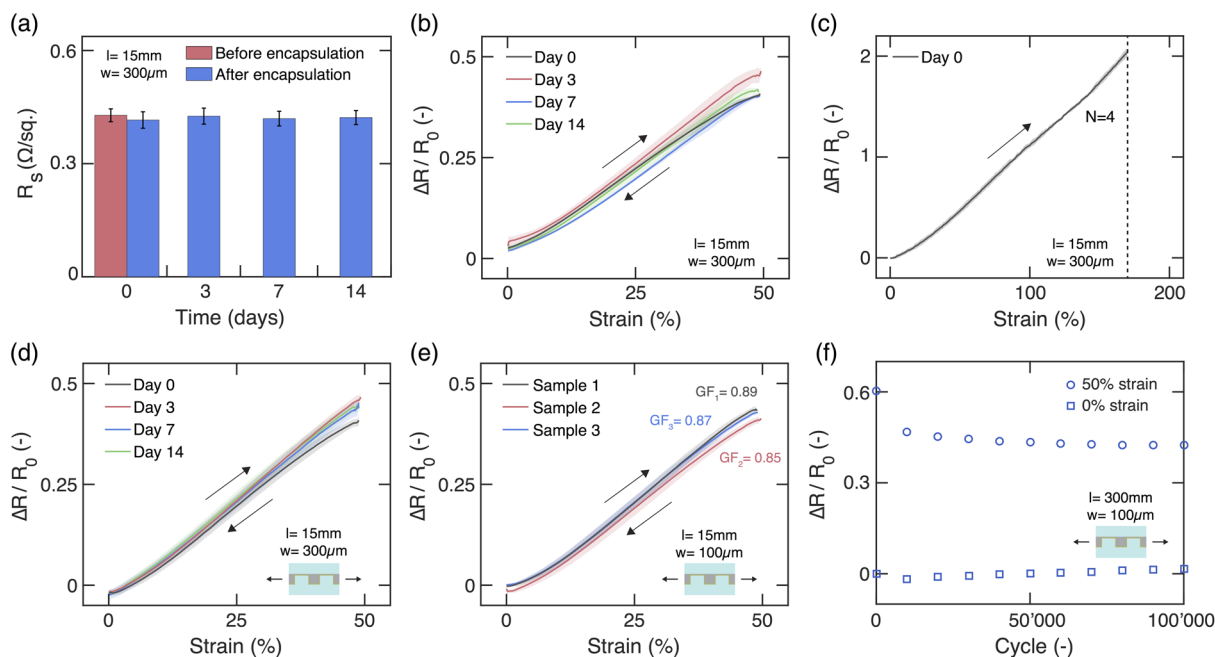


Figure 3. Electromechanical characterization of gallium thin films. a) Electrical sheet resistance of evaporated gallium thin films measured on the wafer before (red) and after (blue) encapsulation at different time intervals (0, 3, 7, and 14 days). The error bars represent SD ($n = 7$). b) Relative change in electrical resistance as a function of strain of non-encapsulated gallium thin films released from the wafer and tested at different time intervals after gallium evaporation (0, 3, 7, 14 days). Each sample was uniaxially stretched to 50% strain for 20 cycles after priming (20 cycles at each strain: 10, 20, 30, and 40%). c) Relative change in electrical resistance as a function of uniaxial loading of non-encapsulated gallium thin films up to 170% strain. The dashed vertical line denotes where mechanical failure of one sample started ($n = 4$). d) Relative change in electrical resistance as a function of strain of encapsulated gallium thin films peeled off the wafer and tested at different time intervals after gallium evaporation (0, 3, 7, and 14 days). Each sample was uniaxially stretched to 50% strain for 20 cycles after priming (20 cycles at each strain: 10%, 20%, 30%, 40%). e) Relative change in electrical resistance as a function of strain of encapsulated gallium thin films peeled off the wafer and tested at different time intervals after gallium evaporation (0, 3, 7, 14 days). Samples were uniaxially stretched to 50% strain for 20 cycles after priming (20 cycles at each strain: 10%, 20%, 30%, 40%, 50%). f) Relative change in electrical resistance over hundred thousand cycles to 50% strain of an encapsulated gallium thin film. The squares and circles represent the values at 0% and 50% strain, respectively.

stretched up to 170% strain, at which point mechanical tearing of the PDMS substrate occurs (Figure 3c). Next, the effect of encapsulation with a 60 μm -thick PDMS layer on the gallium thin film performance was evaluated. Cyclic stretching experiments revealed an electromechanical behavior similar to non-encapsulated substrates (Figure 3d and Figure S11, Supporting Information). This is consistent with scanning electron microscopy (SEM) observations showing that non-encapsulated liquid metal films remain confined within the microstructure during deformation (Video S1, Supporting Information).

Gallium exhibits a low gauge factor^[33], when implemented for strain sensing, patterning tracks with reduced line width is necessary to increase the output sensitivity of the soft sensors. Therefore the electromechanical properties of narrow, 100 μm -wide tracks patterned by photolithography (Figure 3e) were examined. The gallium films stretched reversibly to 50% and the similarity in gauge factor GF (≈ 0.87) across samples confirmed the high reproducibility of the lithography process. In contrast with previous results ($GF \approx 1.5$),^[18] the structured gallium thin films have a lower gauge factor, most likely because of liquid metal rearrangement within the micropillars. Finally, we assessed the high-cycle fatigue resistance of the gallium thin films by uniaxial mechanical loading to 50% strain

for 100 000 cycles (Figure 3f). After an initial decrease in electrical resistance, likely arising from the hysteretic behavior of the gallium oxide skin, the structures displayed durable performance and stabilized electrical conductivity.

The development reported herein demonstrates that precise engineering of the gallium technology enables the integration of thin films that can offer accurate, reproducible, and durable electromechanical properties. To illustrate the potential of the gallium thin film technology suitable in advanced sensing applications, wearable strain sensors were implemented on the human hand to seamlessly and accurately monitor hand movements. Five stick-on gallium sensors are mounted on the hand finger joints and coupled to a virtual-reality model of the hand (Figure 4a). Resistive strain gauges, featuring a meander of twenty parallel 100 μm -wide and 15 mm-long gallium tracks were prepared by photolithography (Figure 4b and Figure S12, Supporting Information). The strain gauges, mounted on the metacarpophalangeal (MCP) and proximal interphalangeal (PIP) finger joints, were connected to a wristband with a wireless module for data transmission. To convert the electrical resistance into the bending angles θ_{MCP} and θ_{PIP} , a simple, fast, and reliable calibration scheme that requires placing the finger joints on objects shaped with precise angles ($\alpha = 60^\circ, 75^\circ, 90^\circ$, and 105°)

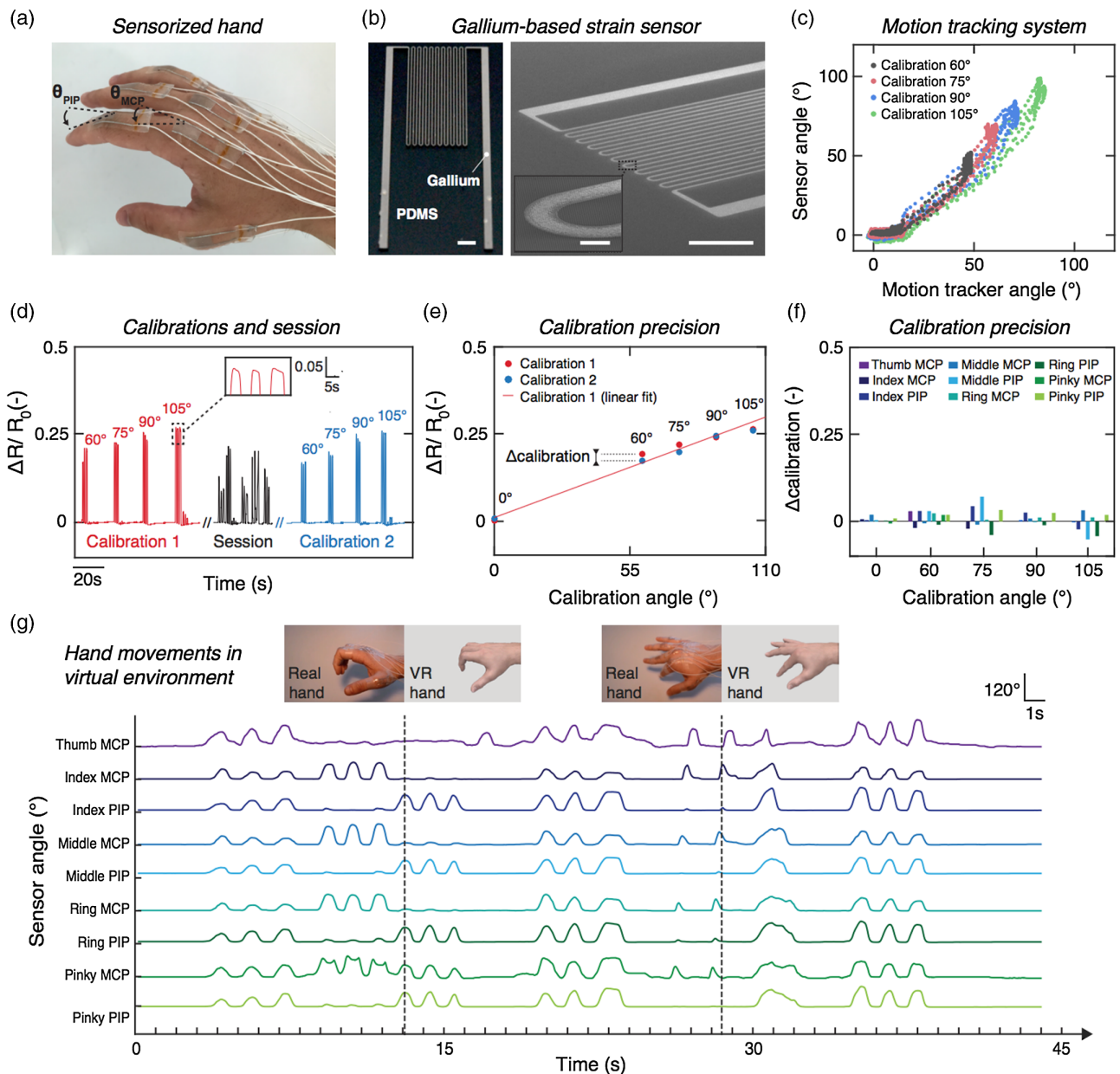


Figure 4. Hand movement tracking for virtual reality applications. a) Photograph of a sensorized human hand where the bending angles of each MCP and PIP joints, θ_{MCP} and θ_{PIP} , are measured by a 100 μm -thick strain sensor. b) Photograph (left) and SEM image (right) of a gallium-based resistive strain sensor featuring a 100 μm -wide, 30 cm-long gallium track. The inset is a close-up view on a meander. Scale bars: 2 mm, 2 mm, and 100 μm , respectively. c) Bending angle measured by the sensor as a function of the angle measured by a camera-based motion tracking system during different bending angle calibrations (60°, 75°, 90°, 105°). d) Relative change in electrical resistance of a sensor monitoring the bending of a finger joint during calibration movements and a recording session. The inset shows three peaks of the curve during a 105° bending angle calibration. e) Relative change in electrical resistance of a sensor as a function of the bending angles during two calibrations and a session in between. f) Deviation between the relative change in electrical resistance of the two calibrations, measured for each calibration angle and nine finger joints. g) Sensed angle as a function of time for nine sensors monitoring the hand movements. The pictures depict the position of the sensorized hand and the associated virtual hand reconstruction at different time points.

(Figure S13, Supporting Information) is proposed. The accuracy of the calibration procedure is characterized with a goniometer. A deviation of $\approx 10\%$ was measured between the calibration object angle and the goniometer angle. The sensor response was then compared after calibration with a camera-based motion tracking system (Figure 4c). Minor deviations of 2°, 10°, 11°, and 11° occur

respectively between the angle measured through calibration ($\alpha = 60^\circ, 75^\circ, 90^\circ$, and 105°) and the angle tracked by the motion reference system. The sensor displays a linear ($R^2 > 0.99$) and reversible behavior to flexion and extension with low hysteresis, a sensitivity of $\approx 7 \Omega / ^\circ$ ($R_0 = 1250 \Omega$), a fast response (delay time $< 20 \text{ ms}$) (Figure S14, Supporting Information), and a low

sensitivity to temperature ($1.34 \Omega / ^\circ\text{C}$) (Figure S15, Supporting Information). In addition, the sensor sustains mechanical loading to 50% strain with high durability (100 000 cycles) (Figure 3f). Furthermore the functionality of the integrated system by recording the kinematics of a freely moving hand and quantifying individual sensor performances are demonstrated with a pre-session calibration and a post-session calibration check (Figure 4d–g and Figure S16, Supporting Information). A comparison of the baseline electrical resistance ($\theta = 0^\circ$) before and after the session indicates that all sensors withstand repetitive flexion and extension movements without major drifts ($\Delta R/R_0 < 2\%$). The precision of the sensors, defined as the angular deviation between the two calibrations averaged on all joints, is 2.4° , 2.6° , 6.6° , 2.3° , and 5.1° for the $\alpha = 0^\circ$, 60° , 75° , 90° , and 105° objects, respectively. The robustness of the sensors and high repeatability of the calibration procedure led us to envision applicability in virtual reality scenarios, where existing hand-monitoring technologies such as data gloves are cumbersome and restrict natural finger motions. We implemented a human-like virtual hand model to replicate the movements measured by our thin, soft, and unobtrusive skin-like system (Figure 4g and Video S2, Supporting Information). The high spatial and temporal coherence between the two hands after synchronization demonstrates the capabilities of gallium-based strain sensors in future health monitoring and gaming applications.

This study presents a microfabrication approach to pattern micrometer-thick gallium films on large-area silicone substrates. By engineering the surface coating and topography of silicone, thin and smooth liquid metal films can be deposited with controlled morphology and well-defined electrical and mechanical properties. The gallium films can be used to produce precise, repeatable, and durable sensing devices. To date, a large variety of sensors based on liquid metal conductors have been proposed to measure finger joint movements.^[11,13–16,19,38,39] However, most of these demonstrations were qualitative, restricted to single or mm-thick devices, or performed on mock-up hand models. In contrast with traditional technologies allowing for tracking of hand movements such as the data gloves, the conformability offered by the thin and soft gallium sensors is of primary importance to preserve natural sensations and avoid movement restrictions. The study demonstrates advanced manufacturing of gallium-based strain sensors combined with robust calibration procedure is paramount to translate laboratory-based innovation into useful soft sensing technology. Future studies will focus on improving the system-level integration by eliminating hard-wired connections and providing additional sensing functionalities such as the adduction and abduction finger movements. Virtual reality was suggested as a possible application scenario for our wearable technology by successfully replicating the movements of a sensorized human hand with a virtual hand model. However, several other opportunities for soft sensing arise in diverse fields such as human–machine interfaces, soft-robotics, and healthcare.^[40]

Experimental Section

Textured PDMS Substrate Fabrication: An illustration of the fabrication process is presented in Figure S1, Supporting Information. A silicon wafer carrier was treated with an adhesion promoter, bis(trimethylsilyl)amine (HMDS), and spin-coated with a $1.5 \mu\text{m}$ -thick (2900 rpm, 45 s) layer of

photoresist (AZ1512, AZ Electronic Materials). After baking (1 min, 110°C), the photoresist was exposed through a photolithography chromium mask with UV light with a dose of with 30 mJ cm^{-2} (MJB4, SUSS MicroTech), developed for 30 s in AZ726 MIF (AZ Electronic Materials), rinsed in de-ionized (DI) water and dried in air. The photoresist mold was then treated with a self-assembled layer of trichloro(1h, 1h, 2h, 2h-perfluorooctyl)silane (Sigma-Aldrich). To form the textured silicone substrate, PDMS (Sylgard 184, Dow Corning) was prepared at a 10:1 ratio of base to curing agent solution by mixing (2 min, 2000 rpm) and defoaming (2 min, 2200 rpm) in a planetary mixer (ARE-250, Thinky), and then spin-coated (800 rpm, 60 s) as a $60 \mu\text{m}$ -thick film on the photoresist mold. After curing for 2 h at 80°C , the PDMS was treated with trichloro(1h, 1h, 2h, 2h-perfluorooctyl)silane (Sigma-Aldrich), spin-coated (250 rpm, 1 min) with a $250 \mu\text{m}$ -thick transfer PDMS layer and cured for 2 h at 80°C . The two PDMS layers were then demolded and transferred upside down to another receiving wafer, which was previously coated with a $60 \mu\text{m}$ -thick liquid PDMS layer. After planarization ($\approx 10 \text{ min}$), the stack was cured for 2 h at 80°C .

Stencil Lithography Patterning of the Gallium Thin Films: A $23 \mu\text{m}$ -thick polyethylene terephthalate (PET) stencil shadow mask (Mylar 23A, Lohmann Technologies) was laser-patterned (MM200-USP, Optec Laser Micromaching Systems) with the desired features and manually laminated on the textured PDMS substrate. A 40 nm -thick gold layer was then sputtered (AC450 CT, Alliance-Concept) on the substrate prior to the thermal evaporation of 2 g of gallium to fill the PDMS substrate textures (E300, Alliance-Concept). The PET mask was gently removed at the end of the process. Gallium thin film tracks with dimensions of $l = 15 \text{ mm}$ and $w = 300 \mu\text{m}$ were patterned using this technique.

Photolithography Patterning of the Gallium Thin Films: Textured PDMS substrates were treated by oxygen plasma for 30 s at 29 W (Diener Electronic) and spin-coated (5000 rpm, 45 s) with an $8 \mu\text{m}$ -thick photoresist layer (AZ9260, AZ Electronic Materials). The photoresist was cured on a hotplate for 12 h at 50°C , exposed through a photolithography chromium mask with UV light with a dose of 300 mJ cm^{-2} (MJB4, SUSS MicroTech), developed for 90 s in a solution of AZ400K diluted in DI water at a 1:5 vol ratio, rinsed with DI water and dried. A 40 nm -thick gold layer was then sputtered (AC450 CT, Alliance-Concept) on the substrate prior to the thermal evaporation of 2 g of Gallium to fill the PDMS substrate textures (E300, Alliance-Concept). The photoresist was removed by lift-off in a solution of SVC-14 (Shipley) for 3 h at 50°C . After rinsing with DI water and drying, the substrate was released from the wafers. Gallium thin film tracks with dimensions of $l = 15 \text{ mm}$ and $w = 100 \mu\text{m}$ were patterned using this technique.

Uniaxial Mechanical Stretching Tests: Rectangular stripes ($12 \times 30 \text{ mm}$) of textured PDMS substrates patterned with the metallization were cut, released from the wafer, and clamped in a customized electromechanical setup (Figure S17, Supporting Information). The two clamps moved along the same axis but in opposite direction so as to deform the sample at a constant velocity rate of $5\% \text{ s}^{-1}$ (five percent of the sample length per second). The electrical resistance was measured with a four-point probe setup (2400 source-meter, Keithley) at 6 Hz with a dedicated LabVIEW program.

PDMS Encapsulation by Spray-Coating: PDMS was prepared at a 10:1 ratio of base to curing agent and diluted with cyclohexane (Sigma-Aldrich) at a 1:4 ratio to decrease its viscosity. After manual mixing and degassing in a desiccator, the solution was spray-coated (Conformal coating tool, Nordson Asymtec) on the gallium thin films with a SC-300 swirl coat applicator nozzle (height: 10 mm, speed: 50 mm s^{-1} , assist pressure: 7.5 psi, fluid pressure: 2.5 psi) to form a $60 \mu\text{m}$ -thick PDMS encapsulation layer, which was successively cured for 2 h at 80°C . The contact pads at the gallium thin film ends were protected with a $23 \mu\text{m}$ -thick polyimide foil (Kapton HN, Lohmann Technologies) to allow for electrical probing.

Scanning Electron Microscopy: Samples were observed with a Hitachi SU5000 microscope using an annular detector with beam energy in the 3–8 keV range.

Strain Sensor Fabrication: The sensors were fabricated according to the aforementioned photolithographic patterning process. The gallium tracks were connected to PTFE stranded wires (Habia) with a drop of eutectic

gallium–indium (EGaIn, Sigma-Aldrich), encapsulated by a silicone sealant (734, Dow Corning) and cured for 12 h at room temperature. The sensors were then encapsulated by spin-coating of a 60 µm (800 rpm, 1 min) PDMS layer and cured for 2 h at 80 °C.

Motion Tracking System Measurements: The position of the markers was recorded at 100 Hz with a Vicon Nexus motion tracking system (Vicon Motion Systems Ltd.) comprising of eight Bonita cameras. The sensor output was measured with a data acquisition device at 3000 Hz (Vicon Datastation ADC Patch Panel). Detailed information is available in Figure S13, Supporting Information.

Recording of the Freely Moving Human Hand: The strain sensors were individually mounted on each of the MCP and PIP finger joints and attached on both extremities with medical tape so as to provide conformability without any movement impediment at the joint location (Figure S16, Supporting Information). During both calibration phases, the joints were individually bent for three repetitions on each of the four calibration objects ($\alpha = 60^\circ, 75^\circ, 90^\circ, 105^\circ$) (Figure S13, Supporting Information). The electrical resistance of the sensors was recorded at 44 Hz and transmitted via a Bluetooth Low Energy wireless module (Qduino Mini, SparkFun Electronics) placed on a wristband. For the hand tracking experiments, informed consent was obtained from the volunteer.

Optical Profilometry: The surface profile and roughness of the gallium thin films were measured with a CountourGt profilometer (Bruker) and analyzed with a dedicated image processing software (Vision64, Bruker).

Mechanical High-Cycle Fatigue Testing: Gallium thin films were stretched to 50% strain for 100 000 cycles at a frequency of 1.3 Hz with a customized stretcher setup. For each 10 000 cycles, the stretcher slowed down to a frequency of 0.14 Hz for 5 cycles, which allowed for recording of the electrical resistance (2400 SourceMeter, Keithley) and sample deformation with a customized LabVIEW program.

Calibration Objects Manufacturing: The four calibration objects were modeled in Solidworks (Dassault Systèmes) and 3D-printed in acrylonitrile butadiene styrene (ABS, uPrint SE, Stratasys).

Supporting Information

Supporting Information is available from the Wiley Online Library or from the author.

Acknowledgements

The authors acknowledge the financial support from the Bertarelli Foundation and SNSF NCCR Robotics. The authors thank L. Albert and G. Reymond (Virtual Reality Facility, Human Neuroscience Platform, Fondation Campus Biotech Geneva) for their help with the virtual hand model, J. Miehlsbradt and S. Micera (Translational Neural Engineering Laboratory, TNE EPFL) for providing support with the motion tracking system, and A. Guillet, V. Ruhaut, and M. Stoeckel (Neuronal Microsystems Platform, Wyss Center) for their support with the microfabrication and characterization facilities.

Conflict of Interest

The authors declare no conflict of interest.

Keywords

liquid metals, motion sensors, stretchable electronics

Received: July 16, 2019

Published online: September 10, 2019

- [1] M. L. Hammock, A. Chortos, B. C. K. Tee, J. B. H. Tok, Z. Bao, *Adv. Mater.* **2013**, 25, 5997.
- [2] T. R. Ray, J. Choi, A. J. Bandodkar, S. Krishnan, P. Gutruf, L. Tian, R. Ghaffari, J. A. Rogers, *Chem. Rev.* **2019**, 119, 5461.
- [3] S. Wagner, S. P. Lacour, J. Jones, P. H. I. Hsu, J. C. Sturm, T. Li, Z. Suo, *Phys. E (Amsterdam, Neth.)* **2004**, 25, 326.
- [4] M. D. Dickey, *Adv. Mater.* **2017**, 29, 1606425.
- [5] H. J. Kim, C. Son, B. Ziaie, *Appl. Phys. Lett.* **2008**, 92, 011904.
- [6] S. Cheng, A. Rydberg, K. Hjort, Z. Wu, S. Cheng, A. Rydberg, K. Hjort, Z. Wu, *Appl. Phys. Lett.* **2016**, 94, 144103.
- [7] H. O. Michaud, L. Dejace, S. De Mulatier, S. P. Lacour, in *IEEE Int. Conf. Intell. Robot. Syst.*, IEEE, Daejeon **2016**, pp. 3186–3191.
- [8] Y. Lu, Q. Hu, Y. Lin, D. B. Pacardo, C. Wang, W. Sun, F. S. Ligler, M. D. Dickey, Z. Gu, *Nat. Commun.* **2015**, 6, 10066.
- [9] T. Liu, P. Sen, C. J. Kim, *J. Microelectromech. Syst.* **2012**, 21, 443.
- [10] Y. Mengüç, Y. L. Park, H. Pei, D. Vogt, P. M. Aubin, E. Winchell, L. Fluke, L. Stirling, R. J. Wood, C. J. Walsh, *Int. J. Rob. Res.* **2014**, 33, 1748.
- [11] R. K. Kramer, C. Majidi, R. Sahai, R. J. Wood, in *IEEE Int. Conf. Intell. Robot. Syst.*, IEEE, San Francisco **2011**, pp. 1919–1926.
- [12] C. Majidi, R. Kramer, R. J. Wood, *Smart Mater. Struct.* **2011**, 20, 105017.
- [13] Y. R. Jeong, J. Kim, Z. Xie, Y. Xue, S. M. Won, G. Lee, S. W. Jin, S. Y. Hong, X. Feng, Y. Huang, J. A. Rogers, J. S. Ha, *NPG Asia Mater.* **2017**, 9, e443.
- [14] S. Kim, J. Oh, D. Jeong, W. Park, J. Bae, *Soft Robot.* **2018**, 5, 601.
- [15] F. L. Hammond, Y. Menguc, R. J. Wood, in *IEEE Int. Conf. Intell. Robot. Syst.*, IEEE, Chicago **2014**, pp. 4000–4007.
- [16] W. Park, K. Ro, S. Kim, J. Bae, *Sensors* **2017**, 17, 420.
- [17] Y. L. Park, B. R. Chen, R. J. Wood, *IEEE Sens. J.* **2012**, 12, 2711.
- [18] J. W. Boley, E. L. White, G. T. C. Chiu, R. K. Kramer, *Adv. Funct. Mater.* **2014**, 24, 3501.
- [19] S. Kim, J. Lee, B. Choi, *IEEE Sens. J.* **2015**, 15, 6077.
- [20] Q. Gao, H. Li, J. Zhang, Z. Xie, J. Zhang, L. Wang, *Sci. Rep.* **2019**, 9, 5908.
- [21] M. D. Dickey, *ACS Appl. Mater. Interfaces* **2014**, 6, 18369.
- [22] C. Ladd, J. H. So, J. Muth, M. D. Dickey, *Adv. Mater.* **2013**, 25, 5081.
- [23] R. A. Bilodeau, D. Y. Zemlyanov, R. K. Kramer, *Adv. Mater. Interfaces* **2017**, 4, 1600913.
- [24] A. Hirsch, L. Dejace, H. O. Michaud, S. P. Lacour, *Acc. Chem. Res.* **2019**, 52, 534.
- [25] Q. Zhang, Y. Gao, J. Liu, *Appl. Phys. A: Mater. Sci. Process.* **2014**, 116, 1091.
- [26] C. Pan, K. Kumar, J. Li, E. J. Markvicka, P. R. Herman, C. Majidi, *Adv. Mater.* **2018**, 30, 1706937.
- [27] B. A. Gozen, A. Tabatabai, O. B. Ozdoganlar, C. Majidi, *Adv. Mater.* **2014**, 26, 5211.
- [28] J. W. Boley, E. L. White, R. K. Kramer, *Adv. Mater.* **2015**, 27, 2355.
- [29] Y. Lin, O. Gordon, M. R. Khan, N. Vasquez, J. Genzer, M. D. Dickey, *Lab Chip* **2017**, 17, 3043.
- [30] M. G. Kim, C. Kim, H. Alrowais, O. Brand, *Adv. Mater. Technol.* **2018**, 3, 1800061.
- [31] G. Li, X. Wu, D. W. Lee, *Sens. Actuators, B* **2015**, 221, 1114.
- [32] K. B. Ozutemiz, J. Wissman, O. B. Ozdoganlar, C. Majidi, *Adv. Mater. Interfaces* **2018**, 5, 1701596.
- [33] A. Hirsch, H. O. Michaud, A. P. Gerratt, S. de Mulatier, S. P. Lacour, *Adv. Mater.* **2016**, 28, 4506.
- [34] L. Courbin, E. Denieul, E. Dressaire, M. Roper, A. Ajdari, H. A. Stone, *Nat. Mater.* **2007**, 6, 661.
- [35] A. Hirsch, S. P. Lacour, *Adv. Sci.* **2018**, 5, 1800256.

- [36] F. Yu, J. Xu, H. Li, Z. Wang, L. Sun, T. Deng, P. Tao, Q. Liang, *Prog. Nat. Sci. Mater. Interfaces* **2018**, 28, 28.
- [37] R. K. Kramer, J. W. Boley, H. A. Stone, J. C. Weaver, R. J. Wood, *Langmuir* **2014**, 30, 533.
- [38] R. Matsuzaki, K. Tabayashi, *Adv. Funct. Mater.* **2015**, 25, 3806.
- [39] M. G. Kim, H. Alrowais, O. Brand, *Adv. Electron. Mater.* **2018**, 4, 1700434.
- [40] M. Amjadi, K. U. Kyung, I. Park, M. Sitti, *Adv. Funct. Mater.* **2016**, 26, 1678.